Materials Horizons

Heterointerface optimization in covalent organic framework-on-MXene for high-performance capacitive deionization of oxygenated saline water

Journal:	*Materials Horizons*
Manuscript ID	MH-COM-11-2021-001882.R3
Article Type:	Communication
Date Submitted by the Author:	20-Mar-2022

Complete List of Authors:	Zhang, Shuaihua; Agricultural University of Hebei, College of Science Xu, Xingtao; National Institute for Materials Science, MANA Liu, Xiaohong; National Institute for Materials Science, International Center for Materials Nanoarchitectonics (WPI-MANA) Yang, Qian; Hebei University Shang, Ningzhao; Agricultural University of Hebei, College of Science Zhao, Xiaoxian; Agricultural University of Hebei, College of Science Zang, Xiaohuan; Hebei Agricultural University, Science Wang, Chun; Hebei Agricultural University Wang, Zhi; Agricultural University of Hebei, College of Science Shapter, Joe; The University of Queensland - Saint Lucia Campus, Yamauchi, Yusuke; University of Queensland, School of Chem Eng and AIBN

Conceptual Insights Statement

One of the biggest challenges limiting practical application of capacitive deionization (CDI) is the low desalination performance of the electrode materials in natural (oxygenated) saline water. In this contribution, we report the heterointerface optimization in MXene-organic hybrid materials to maximize the CDI performance of MXene-based materials in oxygenated saline water. Through pioneering homologous monomer-mediated hydrogen bonding assembly of MXene ($Ti_3C_2T_x$) with β-keto-enamine-linked covalent organic frameworks (COFs), a core-shell MXene@COF heterostructure, different from other related materials, not only maintains the unique 2D architecture as well as excellent electron conductivity of MXene, but also features large porosity, high Na^+ adsorbability and good inoxidizability like COFs. As expected, the obtained CDI performance in oxygenated saline water is among the state of the art of CDI electrodes and better than most of 2D materials. This strategy highlights the significance of heterointerface optimization and the importance of inorganic-organic hybridization, and also accelerates the development of practical CDI application.

Heterointerface optimization in covalent organic framework-on-MXene for high-performance capacitive deionization of oxygenated saline water

Shuaihua Zhang,[‡a,b] Xingtao Xu, [‡*b] Xiaohong Liu,[b] QianYang,[c] Ningzhao Shang,[a] Xiaoxian Zhao,[a] Xiaohuan Zang,[a] Chun Wang,[a] Zhi Wang,[a] Joseph G. Shapter[d] and Yusuke Yamauchi[*b,d]

[a] *Department of Chemistry, Hebei Agricultural University, Baoding 071001, Hebei, China.*

[b] *International Center for Materials Nanoarchitectonics (WPI-MANA), National Institute for Materials Science (NIMS), 1-1 Namiki, Tsukuba, Ibaraki 305-0044, Japan. E-mail: Xu.Xingtao@nims.go.jp*

[c] *College of Public Health, Hebei University, Baoding 071002, Hebei, China*

[d] *Australian Institute for Bioengineering and Nanotechnology (AIBN), The University of Queensland, Brisbane, QLD 4072, Australia. E-mail: y.yamauchi@uq.edu.au*

[‡] *The authors contributed equally to this study.*

Abstract

Capacitive deionization (CDI) provides a promising option to provide affordable freshwater with simultaneously storing energy, but its scale application is usually limited owing to the poor performance of conventional materials in natural (oxygenated) saline water. Herein, we report a heterointerface optimization in covalent organic framework (COF)-on-MXene heterostructure achieving a high CDI performance for desalination of oxygenated saline water. The 2D heterostructure with optimal core-shell architecture inherits high conductivity, and reversible ion intercalation/deintercalation ability of MXene and the hierarchical porous structure, large porosity, and extraordinary redox capacity of COFs. Thanks to the heterointerface optimization, MXene@COF heterostructure exhibits a very stable cycling performance over 100 CDI cycles with a maximum NaCl adsorption capacity of 53.1 mg g^{-1} in oxygenated saline water, among the state-of-the-art values for CDI electrodes and also exceeding those of most MXene-based or 2D materials. This study highlights the importance of heterointerface optimization in MXene-organic 2D heterostructures to promote CDI of natural (oxygenated) saline water.

Introduction

Capacitive deionization (CDI), an electrochemical methodology that desalts water with simultaneously storing energy through electrosorption[1-3] or redox reactions,[4-6] has emerged as an attractive option to provide affordable water with low energy consumption and high output efficiency.[7-11] Porous carbons, featured with high porosity and favorable conductivity, have been the preference in CDI electrode materials for many years.[2,12,13] Unfortunately, most carbons usually have low salt adsorption capacity (SAC) and poor cycling stability in natural (oxygenated) saline water,[14, 15] consequently limiting the development of CDI to a new stage. Within this context, two-dimensional (2D) transition metal carbides and nitrides, collectively referred to as MXenes, have received increasing interests for diverse electrochemical interfaces in CDI and other energy storage devices[16-21] due to high electrochemical capacity,[22] excellent electrical conductivity, good reversible ion intercalation/deintercalation,[18] and hydrophilic surfaces with plentiful Lewis acid Ti sites and –OH (–F, –O, *etc.*) groups.[23-25] However, MXene nanosheets are generally subject to inevitable aggregation and self-restacking owing to the intense van der Waals interactions between adjacent nanosheets,[26, 27] and also exhibit poor stability in natural saline water due to the interaction of water and oxygen in the surrounding environment,[28] which considerably limit their performance and lifetime for CDI applications.

MXene-organic 2D heterostructure might be used to address challenges related to self-restacking and poor oxidation stability of MXene.[28] In particular, the combination of covalent organic frameworks (COFs), a famous organic material whose derivatives have favorable CDI performance and good stability,[29] with MXenes may bring new features from COFs, including high porosity, redox activity, *etc.* and meanwhile, prevent the MXene nanosheets from stacking/self-oxidization problem if the COFs could be perfectly coated on MXene surface. Very recently, the synthesis of MXene/COF composites/hybrids has been developed by using one-step ionothermal catalytic[30] or heterologous linker-mediated covalent assembly strategies.[31, 32] However, these obtained MXene/COF materials were mostly aggregated or lacking well-preserved heterointerface between each component possibly due to competitive hydrogen bonding effect during the assembly process of COFs on MXene nanosheets. In this regard, the resulting MXene/COF materials with exposed MXene surface will be easy to oxidize, leading to serious performance deterioration and further limiting their potential applications in CDI.

In this contribution, we report a heterointerface optimization in MXene@COF 2D heterostructure *via* homologous monomer-mediated hydrogen bonding assembly of MXene ($Ti_3C_2T_x$) with *β*-ketoenamine-linked COF (2,6-diaminoanthraquinone-1,3,5-triformylphloroglucinol-COF, DAAQ-TFP-COF). The prepared heterostructure maintains the unique 2D architecture and excellent electron conductivity of MXene, but also features a large specific surface area (SSA) and hierarchical porous structure, like that of COFs, which are indispensable for CDI.[33] The outer COF layers prevent the MXene nanosheets from restacking and becoming oxidized and therefore protect the MXene from activity degradation during desalination/regeneration. The inner MXene nanosheets, which act as the substrate, enable the reversible transport of electrons and ions, and simultaneously improve the conductivity of the COF nanostructures. More importantly, COF nanostructures with the redox-active DAAQ building monomers can contribute to extraordinary Faradaic Na^+ adsorbility, affording short Na^+ diffusion pathways and additional redox active sites for high Na^+ capture. As revealed by experimental and theoretical analysis, the optimal heterointerface endows the MXene@COF heterostructure with high CDI performance with state-of-the-art SAC and good cycling stability.

Results and Discussion

Heterointerface Optimization Principle. The inorganic-organic heterointerface optimization in MXene@COF heterostructure is schematically illustrated in **Scheme 1A**. First, $Ti_3C_2T_x$ MXene nanosheets were produced from Ti_3AlC_2 by selectively etching the metallic Al-Ti bonds with LiF/HCl.[26] The freshly synthesized MXene nanosheets were then modified with a building (homologous) monomer of DAAQ-TFP-COF, that is, DAAQ, by hydrogen bonds to form a monodispersed DAAQ-functionalized MXene (denoted as MXene-NH_2, Step I in **Scheme 1A**). Subsequently, the DAAQ-TFP-COF nanoarrays were vertically anchored on the surface of MXene-NH_2 precursors by the covalent linking of DAAQ and TFP with a Schiff-base condensation reaction (Step II in **Scheme 1A**) to obtain a monodispersed MXene@COF sandwich nanoarchitecture. In particular, the pre-grafting of the homologous DAAQ monomer on the surface of the MXene nanosheets is crucial for the controlled growth of the uniform crystalline COF nanoarrays on the 2D nanosheets. In a preliminary effort, we tried to directly assemble the COF nanoarrays on MXene without DAAQ modification. Unfortunately, we observed only the

aggregation of MXene nanosheets and self-assembled uncontrollable bulk COFs rather than uniform COF nanoarrays on the surface of the MXene nanosheets (**Fig. S1**), possible due to the competitive hydrogen interactions between DAAQ and TFP on MXene surfaces. To address this issue, we introduced a homologous monomer DAAQ to mediate MXene surface forming DAAQ-functionalized MXene surface for the controllable growth of COF nanoarrays *via* further covalent bonding assembly. Because the MXene surface has a large number of terminal groups such as –F, –O, and –OH, hydrogen bonding interactions[34-36] ensured that the DAAQ molecules were tightly bound on the MXene surface to obtain modified MXene nanosheets with abundant $–NH_2$ groups. The pre-grafted DAAQ building blocks not only act as a bridge between the inner MXene nanosheets and the outer COF layers, which afford better interaction, but also offer many nucleation centers for the covalent bonding of the COFs, which improves the uniformity of the DAAQ-TFP-COF on MXene forming an optimal heterointerface. We also noted there exist several other MXene/COF examples prepared by utilizing heterologous linker to pre-modify MXene surface *via* covalent bonds for further growth of COFs,[42, 43] but the obtained hybrids are usually aggregated without uniform COF coating on MXene nanosheets possibly due to the majority of hydrogen bonding interactions during COF growth. Finally, the obtained MXene@COF 2D heterostructures exhibit several unique structural advantages such as antioxidation ability, electron conductivity, and Na^+ adsorbility, making them highly suitable for CDI applications (**Scheme 1B**).

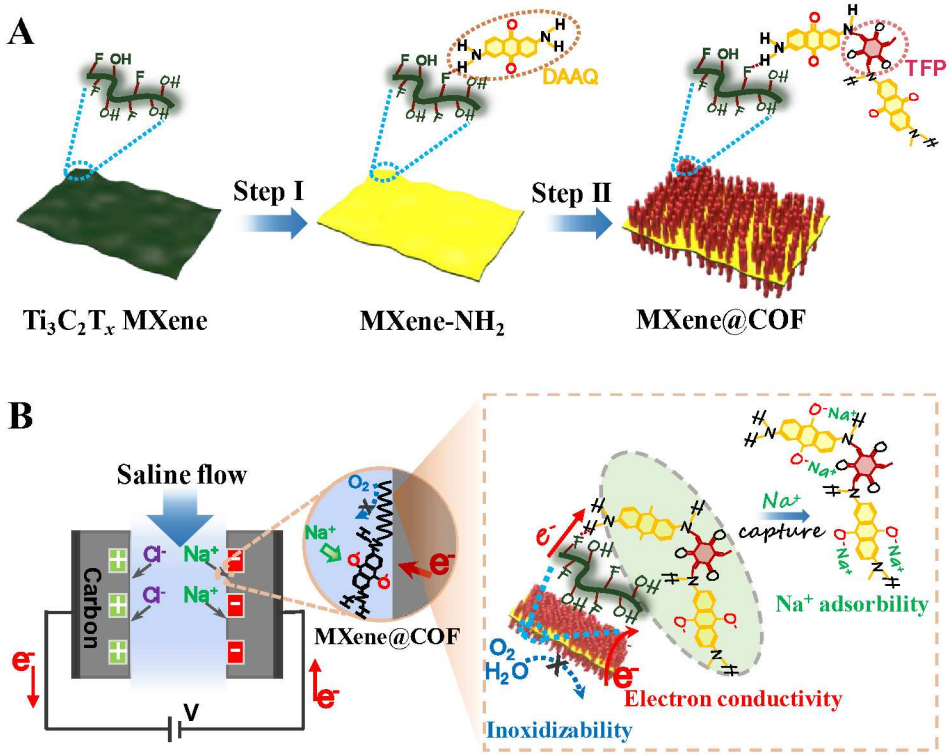

Scheme 1. Schematic illustration for heterointerface optimization in MXene@COF heterostructure and its promotion on CDI process. (A) Heterointerface optimization process includes (I) $Ti_3C_2T_x$ MXene synthesized from MAX phase Ti_3AlC_2 using a LiF/HCl etching was modified by the DAAQ molecules *via* hydrogen bonding, and (II) the resulting MXene-NH_2 was employed for constructing MXene@COF heterostructure by covalently linking TFP with DAAQ through a convenient Schiff-base condensation reaction. (B) Promotion of optimized MXene-COF heterointerface on CDI process, including antioxidation, electron conductivity, and Na^+ adsorbility.

Morphological and physical properties. The morphology and microstructure of pristine MXene, MXene-NH_2, and the MXene@COF 2D heterostructure were characterized by scanning electron microscopy (SEM) and transmission electron microscope (TEM). **Fig. 1A** and **S2A-C** show SEM and TEM images of the pristine MXene nanosheets, which have a clean surface and well-defined edges; no accordion-like architecture is observed, suggesting that the MXene nanosheets have been successfully exfoliated. The selected area electron diffraction (SAED) pattern (**Fig. S2C**, inset) reveals a hexagonal atomic arrangement, in agreement with previous reports on $Ti_3C_2T_x$ MXene nanosheets.[37] After functionalization with the monomer DAAQ (0.15 mM) of the COF, the monodispersed MXene-NH_2-(0.15 mM) nanosheet similar to that of the pristine MXene precursors is preserved

(**Fig. 1B** and **S2D**). The successful assembly of DAAQ-TFP-COF on the MXene-NH_2-(0.15 mM) is confirmed by the SEM and TEM images in **Fig. 1C, D** and **S3**, suggesting that DAAQ-TFP-COFs with a nanofiber structure, similar to the pristine DAAQ-TFP-COF (**Fig. S4**), are vertically anchored on both sides of the MXene flakes to form a core-shell MXene@COF architecture. In particular, the enlarged view of the heterostructure in **Fig. 1E** clearly reveals that the COF nanoarrays fully cover the MXene surface (dark area) to form a core-shell architecture with well-preserved heterointerface. The HRTEM image in **Fig. 1F** further reveals lattice fringes with an interlayer spacing approximately 0.26 nm, which are attributed to the (100) lattice planes of the $Ti_3C_2T_x$ MXene. Moreover, the high-angle annular dark field (HAADF) image and the corresponding elemental mapping images (**Fig. 1G**) show a uniform distribution of C, O, Ti, and F in the heterostructure. In contrast, when a lower monomer DAAQ concentration (0.03 mM) is employed to functionalize the MXene nanosheets, the obtained MXene-NH_2-(0.03 mM) nanosheets have similar nanosheet morphologies with the MXene-NH_2-(0.15 mM) (**Fig. S5A**). However, when further used for growing DAAQ-TFP-COF, the well-defined heterointerface in MXene@COF cannot be achieved (**Fig. S5B**) since the MXene-NH_2-(0.03 mM) might be lack of sufficient growth sites for the uniform growth of COFs.

Furthermore, the heterointerface optimization in MXene@COF heterostructure was also studied in aspects of the effect of the COF precursor concentrations (**Fig. S6**). As clearly revealed by SEM observations, when the concentration of the COF precursor is low (TFP, 0.02 mM; DAAQ, 0.03 mM), the obtained hybrid, denoted as MXene@COF-low, consists of 2D nanosheets with short oriented COF nanorods uniformly deposited on the MXene surface (**Fig. S6A, B**); however, owing to the low COF content, the entire MXene surface is not effectively covered, failing to obtain a well-preserved heterointerface which might result in the oxidization of MXene nanosheets during CDI in natural (oxygenated) saline water. Furthermore, excessive COF precursor concentrations (TFP, 0.4 mM; DAAQ, 0.6 mM), referring to the sample labeled MXene@COF-high, will result in the formation of longer COF nanofibers with a thicker layer and severe agglomeration of the nanosheets (**Fig. S6C, D**), which will be unfavorable for electrolyte access and ion diffusion. **Fig. S7** shows that both MXene@COF-low and MXene@COF-high have lower CDI performances than MXene@COF (TFP, 0.1 mM;

DAAQ, 0.15 mM), suggesting that the precursor concentrations for optimal heterointerface are 0.1 mM for TFP and 0.15 mM for DAAQ.

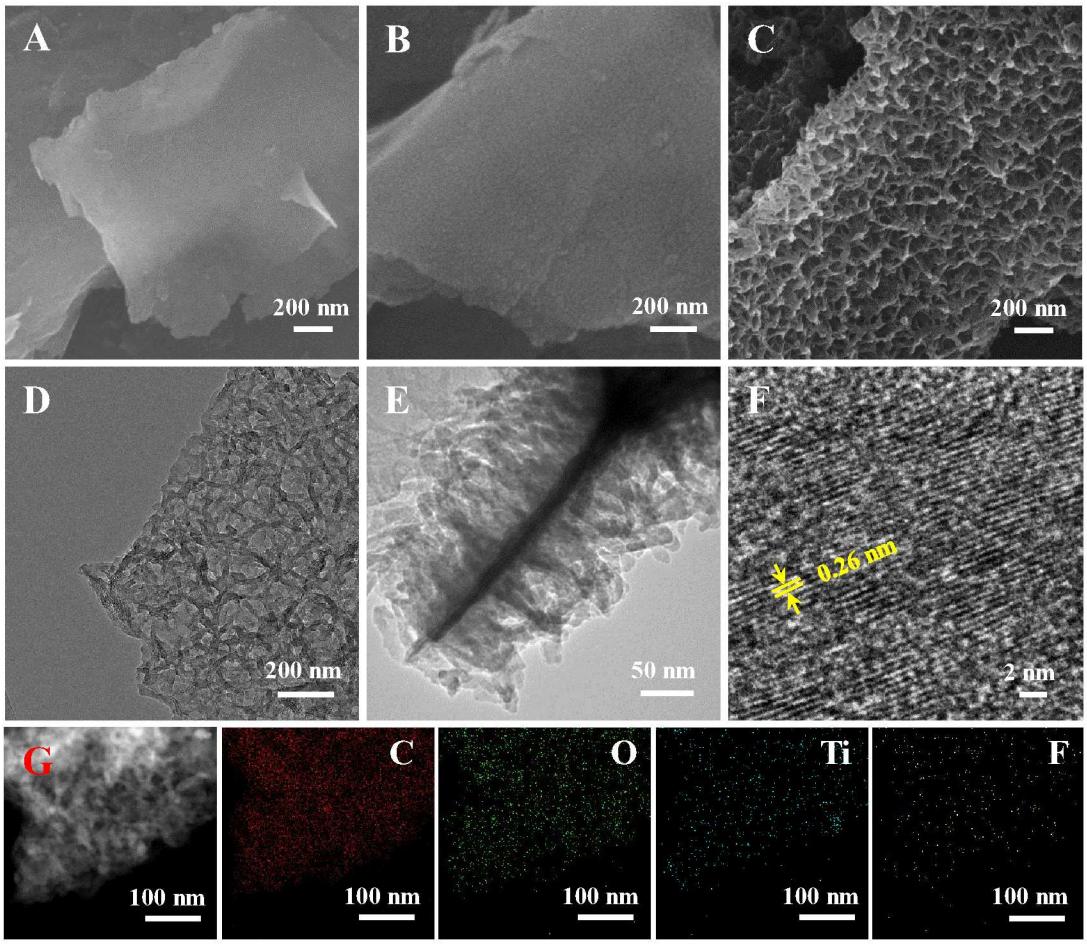

Fig. 1. Morphological characterization of MXene@COF 2D heterostructure. (A) SEM image of pristine $Ti_3C_2T_x$ MXene nanosheets. (B) SEM image of DAAQ-functionalized MXene-NH_2. (C) SEM, (D, E) TEM, and (F) HRTEM images of MXene@COF 2D heterostructure. (G) HAADF-STEM image of MXene@COF 2D heterostructure with elemental mappings of C, O, Ti, and F.

Fourier transform infrared spectroscopy (FTIR) was conducted to investigate the formation of COFs on MXene nanosheets. **Fig. S4D** clearly shows the complete elimination of the starting monomers, as indicated by the disappearance of the N–H stretching bands of the DAAQ monomer (3100–3300 cm^{-1}) and the –CHO stretching bands of the TFP monomer (~2913 cm^{-1}).[38-40] The intense peaks of the DAAQ-TFP-COF at 1560 cm^{-1} (C=C) and 1250 cm^{-1} (C–N) (**Fig. 2A**) reveal the successful formation of β-ketoenamine linked framework structures, in agreement with previous reports.[38-40] When MXene nanosheets are functionalized by DAAQ, the

characteristic peaks of NH_2 and C=O can be observed in the FTIR spectrum of DAAQ-functionalized MXene-NH_2 in comparison with pristine MXene (**Fig. S8**). With regards to MXene@COF, the characteristic absorption peaks from C=C and C–N vibrations shift to slightly higher wavelengths (1574 and 1261 cm^{-1}, respectively), indicating the possible formation of hydrogen bonds between the functional groups of the MXene nanosheets and the DAAQ groups of the COF.[41] The FTIR spectrum of pristine MXene exhibits O–H and C−O stretching vibrations at 3417 and 1108 cm^{-1}, respectively. The intensity of O–H vibration in the FTIR spectrum of the MXene@COF heterostructure is significantly lower than that of pure MXene, which is attributed to the fact that the MXene nanosheets are well encapsulated by the COF macromolecules because of the hydrogen bonds.[41, 42] The ^{13}C NMR spectrum of the MXene@COF heterostructure (**Fig. S9**) shows that the strong peak at approximately 146 ppm can be ascribed to the enamine carbon atom (=C–NH–), confirming the successful formation of the β-ketoenamine-linked DAAQ-TFP-COF in the heterostructure.[43, 44] The X-ray diffraction (XRD) pattern of pure DAAQ-TFP-COF displays two main characteristic peaks at ~3.6° and ~26.0°, which correspond to the reflections from the (100) and (002) planes, respectively (**Fig. 2B**). From the *d* spacing of the (002) peaks, we calculated an interlayer π–π stacking distance between the individual COF layers of 3.6 Å (**Fig. S4C**). The experimental XRD patterns are in good agreement with the simulated AA eclipsed stacking models of DAAQ-TFP-COF, which are also in agreement with previous studies.[38-40] The XRD pattern of the MXene@COF heterostructure shows not only the characteristic COF peaks, but also the (002) peak belonging to the $Ti_3C_2T_x$ MXene. Interestingly, the (002) diffraction peak shifts from 7.2° for the pristine MXene to 6.34° for the MXene@COF heterostructure after the introduction of DAAQ-TFP-COF, indicating an increased interlayer spacing after MXene-COF heterointerface formation.

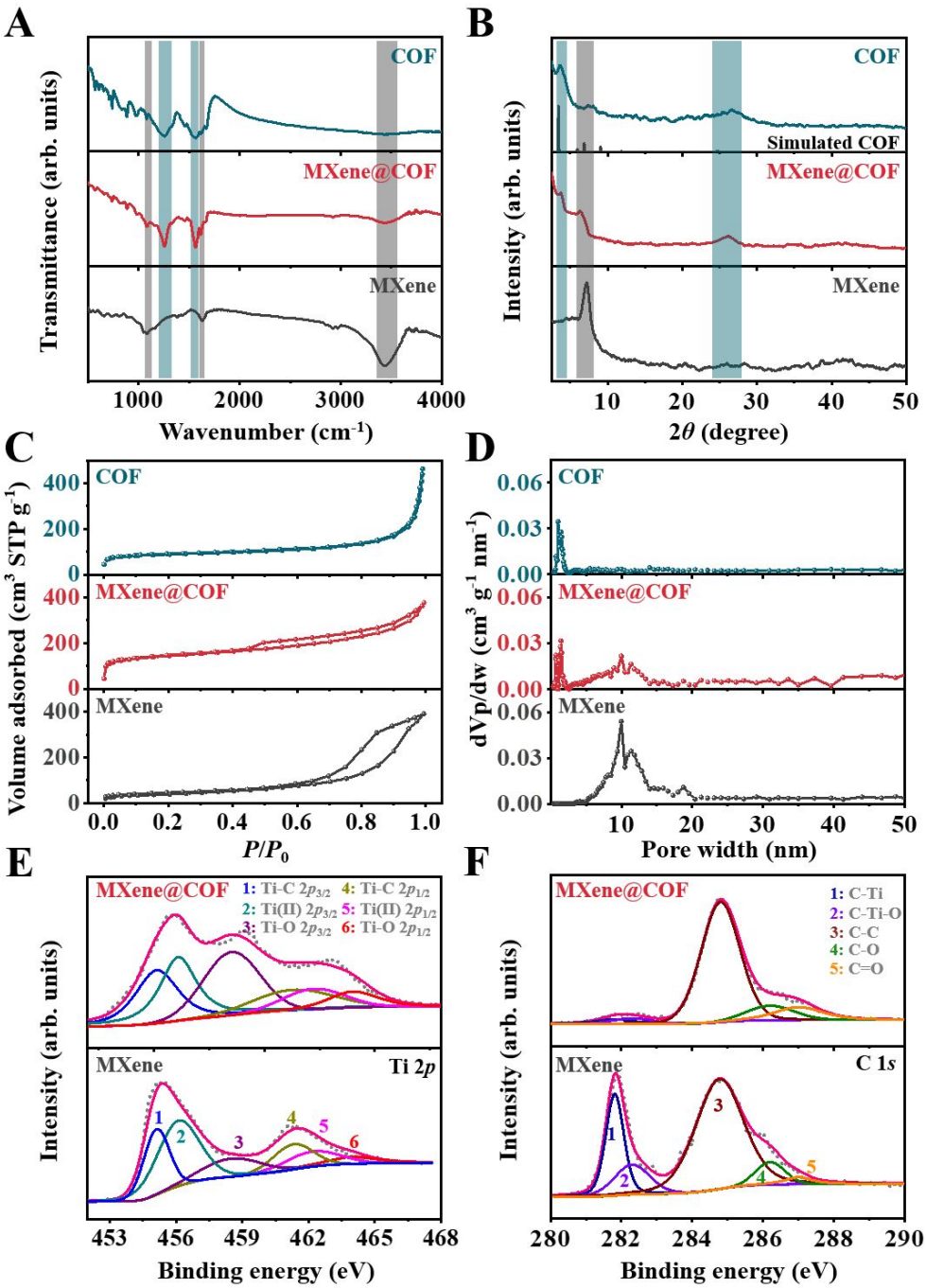

Fig. 2. Material characteristics of MXene@COF heterostructure. (A) FTIR spectra of pure MXene, DAAQ-TFP-COF, and MXene@COF heterostructure. (B) Experimental and simulated XRD patterns of DAAQ-TFP-COF, pure MXene, and MXene@COF heterostructure. (C) N_2 adsorption–desorption isotherms and (D) pore size distributions of pure MXene, DAAQ-TFP-COF, and MXene@COF heterostructure. (E) Ti 2*p* and (F) C 1*s* spectra of pure MXene and MXene@COF heterostructure.

The nitrogen adsorption–desorption isotherms of the pure MXene, DAAQ-TFP-COF, and MXene@COF heterostructure were obtained to investigate their porous structure and SSA (**Fig. 2C**, **D**, and **S10A**). The pure MXene has a low SSA of only 155 $m^2 g^{-1}$, while the MXene@COF heterostructure exhibits a significantly higher SSA of up to 424 $m^2 g^{-1}$, which might be attributed to the unique 2D sandwich structure of MXene@COF and synergistic effects between MXene nanosheets and porous COFs. Moreover, the nonlocal density functional theory (DFT) pore size distribution plots show distinct peaks for micro- and mesopores.[45] The cumulative pore size distributions in **Fig. S10B** further reveal that the micro- and mesopores of MXene@COF are corresponded with large pore volumes, which is favorable for high CDI performance. The thermogravimetric analysis curves in **Fig. S11** further show that the MXene@COF heterostructure has a better thermal stability than pure DAAQ-TFP-COF.

The X-ray photoelectron spectroscopy (XPS) survey spectra in **Fig. S12** reveal that the MXene@COF heterostructures are composed mainly of C, O, N, Ti, and F, with stronger C 1*s* and N 1*s* signals than pure MXene owing to the introduction of DAAQ-TFP-COF. Compared with pure MXene, the intensity of the titanium (Ti 2*p*) and fluorine signals in the heterostructure is significantly lower, suggesting that the DAAQ-TFP-COF layers almost completely cover the MXene surface. The high-resolution Ti 2*p* XPS spectra (**Fig. 2E**) can be fitted using the contributions of three doublets (Ti $2p_{3/2}$–Ti $2p_{1/2}$),[26, 27] and the Ti $2p_{3/2}$ components located at 455.1, 456.1, and 458.5 eV correspond to Ti–C, Ti(II), and Ti–O bonds, respectively. The Ti–O peak of MXene@COF accounts for a larger percentage than that of pure MXene. Generally, the Ti–O oxide peak (458.5 eV) is ascribed to the formation of TiO_2;[26, 27] however, the XRD pattern (**Fig. 2B**) shows no obvious peaks for TiO_2, and the Raman spectrum of MXene@COF shows similar vibrations in a Raman shift range of 100–750 cm^{-1} (**Fig. S13**), suggesting that the increase in the intensity of the Ti–O oxide peak is due mainly to possible interaction between MXene and the quinone groups of the COF nanosheets.[27, 41] The C 1*s* core level spectra (**Fig. 2F**) could be fitted with five components centered at 281.8, 282.3, 284.8, 286.2, and 287.0 eV, which were assigned to C–Ti, Ti–C–O, C–C, C–O, and C=O bonds, respectively. These results demonstrate that the heterostructure consists of MXene and COF components, and the retained intrinsic structure of MXene nanosheets is expected to endow the MXene@COF heterostructure with high electrical conductivity.

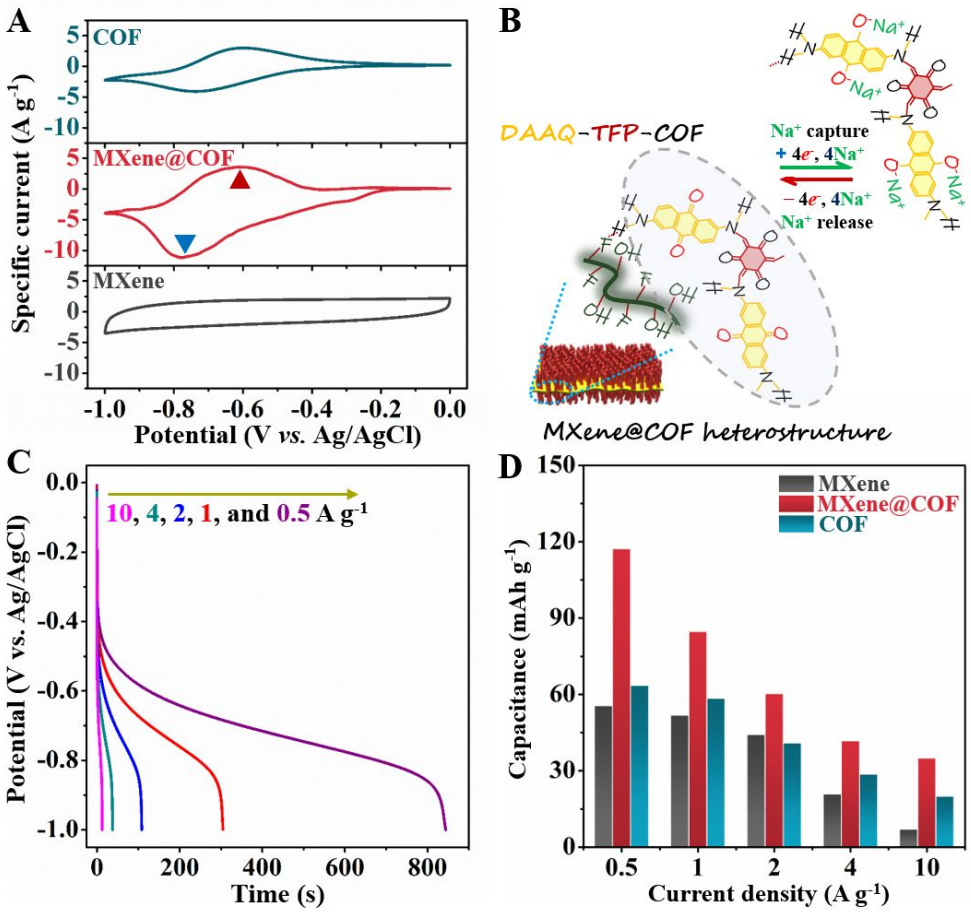

Fig. 3. Electrochemical properties of MXene@COF heterostructure. (A) CV curves of pure MXene, pure COF, and MXene@COF heterostructure at 10 mV s^{-1}. (B) Schematic illustration of electrochemical redox reactions between Na^+ of NaCl electrolyte and quinone groups in DAAQ-TFP-COF. (C) Discharge curves of MXene@COF heterostructure at specific currents ranging from 0.5 to 10 A g^{-1}. (D) Specific capacitance versus specific current for pure MXene, pure COF, and MXene@COF heterostructure.

Electrochemical properties. The MXene@COF heterostructure has a high SSA, fascinating 2D architecture, excellent conductivity owing to the presence of the MXene, and abundant redox-active groups within the frameworks. Thus, it should have superior electrochemical properties for CDI application. The electrochemical performance of the MXene@COF heterostructure was first measured using a three-electrode configuration in a 1 M NaCl electrolyte with a potential range of −1.0 to 0 V. The cyclic voltammetry (CV) curves in **Fig. 3A** clearly show the presence of a pair of quasi-reversible redox peaks within the curves of the COF and MXene@COF heterostructure, which correspond to the quinone/hydroquinone redox process of the DAAQ groups with the Na^+

ions of NaCl electrolyte (**Fig. 3B**), suggesting that the DAAQ groups provide the COF and MXene@COF heterostructure with good reversible capture/release of Na^+ for potential CDI application.

In addition, the integrated area of the CV curve of the MXene@COF heterostructure is larger than those of pure MXene and pure COF, indicating better capacitive performance and higher capacitance, which should be attributable to the novel advantages of the MXene@COF heterostructure. The discharge curves of the MXene@COF heterostructure at various specific currents (0.5–10 A g^{-1}) in **Fig. 3C** further demonstrate the pseudocapacitive behavior of the heterostructure, which has significantly longer discharge time compared to that of pure MXene or COF (**Fig. S14**) at any specific current, further confirming that the heterostructure offers the highest charge capacity. **Fig. 3D** shows the corresponding specific capacities of the MXene, COF, and MXene@COF heterostructure at various specific currents. As expected, the MXene@COF heterostructure exhibits the highest capacity at any specific current, suggesting that it is capable of good CDI performance. **Fig. S15** compares the Nyquist plots derived from the electrochemical impedance spectroscopy (EIS) measurements of the MXene@COF heterostructure and COF. The charge transfer resistance, R_{ct}, of the MXene@COF electrode (2.4 Ω) is obviously lower than that of the pure DAAQ-TFP-COF electrode (**Fig. S15**), which indicates an improved electronic conductivity *via* the heterointerface optimization, ensuring its excellent electrochemical performance.

CDI performance in oxygenated saline water. Higher capacitive performance generally corresponds to better CDI performance. The MXene@COF heterostructure was assembled to the CDI cells (**Fig. S16**) with MXene@COF as cathode (mass loading: 2 mg cm^{-2}) while AC (mass loading: 2 mg cm^{-2}) as anode, and their CDI performance was evaluated in NaCl solution with initial concentrations of 500 and 1000 mg L^{-1} at 1.2 V. **Fig. 4A** and **S17A** show the SAC *versus* time for the MXene, COF, and MXene@COF heterostructure; the SAC values increase until they almost reach equilibrium at 30 min. The MXene@COF heterostructure has the high SAC values of 24.5 mg g^{-1} at 500 mg L^{-1} and 37.2 mg g^{-1} at 1000 mg L^{-1}, whereas those of pure MXene and COF are 18.6 (at 500 mg L^{-1})/28.2 (at 1000 mg L^{-1}) and 13.5 (at 500 mg L^{-1})/20.4 (at 1000 mg L^{-1}) mg g^{-1}, respectively. The heterostructure even significantly outperforms the commercial benchmark performance by activated carbon

(AC; 10.4 mg g^{-1} at 500 mg L^{-1} and 15.6 mg g^{-1} at 1000 mg L^{-1}), indicating the excellent potential of our MXene@COF heterostructure for commercial application. **Fig. S17B** further reveals that the MXene@COF heterostructure achieves both larger values in SAC and areal SAC than those of pure MXene, COF and AC. What's more, the MXene@COF heterostructure also possesses the largest charge efficiency among the samples (**Fig. S17C, D**), possibly suggesting the introduction of COF layer indeed could effectively prevent the co-ion expulsion effect to some extent. **Fig. 4B** shows the corresponding CDI Ragone plots of MXene, COF, the MXene@COF heterostructure, and AC; that of the heterostructure clearly shows a shift toward the upper right, indicating better desalination performance and rate. Furthermore, the CDI performance of MXene, COF, and the MXene@COF heterostructure were investigated at operating voltages ranging from 1.0 to 1.6 V (**Fig. 4C** and **S18**). The SAC clearly increases with increasing operating voltage, and the MXene@COF heterostructure achieves a very high SAC of 53.1 mg g^{-1} at 1.6 V (at 1000 mg L^{-1}), which is better than most of the MXene-related materials and even comparable to some state-of-the-art values for other faradic CDI materials (**Table S1**). Even in 600 mM NaCl solution, our MXene@COF heterostructure also keeps a high SAC of 72.0 mg g^{-1} (**Fig. S19**), like most MXene-based materials demonstrated by Presser group and others.[28, 46, 47] Such a high CDI performance for heterostructure can be ascribed to the optimal heterointerface in MXene@COF, which brings the high Na^+ adsorbility to the MXene material system (**Fig. S20**). Notably the potential of such a CDI cell for storing electric energy has also been demonstrated in **Fig. S21**, which shows the cell can lighten the LED light during electrode regeneration (discharging) process, suggesting the ability of our CDI apparatus to store energy.

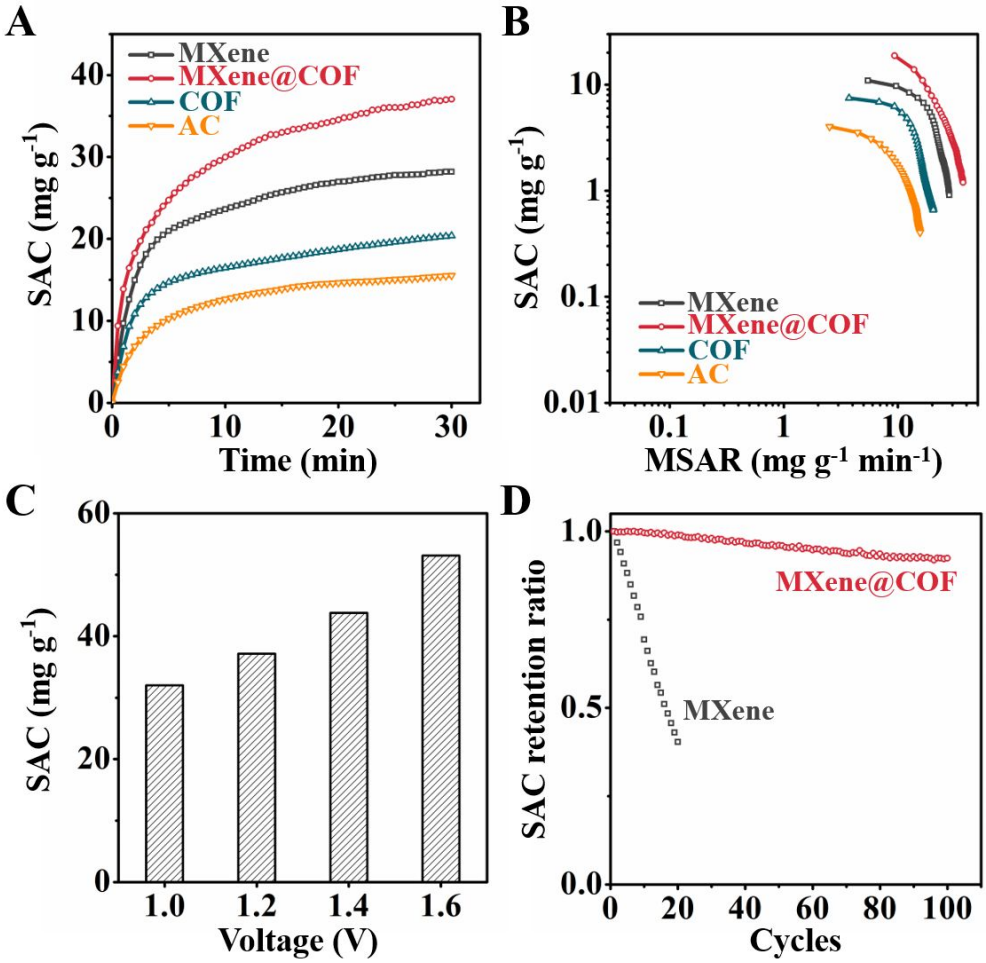

Fig. 4. CDI profiles of MXene@COF heterostructure in oxygenated NaCl solution. (A) SAC versus time and (B) corresponding CDI Ragone plots, *i.e.*, SAC *versus* mean salt adsorption rate at *t* min (MSAR, mg g^{-1} min^{-1}), for MXene, COF, MXene@COF heterostructure, and AC at 1.2 V in 1000 mg L^{-1} NaCl solution. (C) SAC of MXene@COF heterostructure at various operation voltages in 1000 mg L^{-1} NaCl solution. (D) CDI cycling performance of MXene and the MXene@COF heterostructure at 1.2 V in 1000 mg L^{-1} NaCl solution.

In order to further investigate the structural advantages of the MXene@COF 2D heterostructure, two samples, that is, the as-prepared MXene/COF hybrid (**Fig. S1** and **S22A, B**) and a physical mixture of MXene and COFs (denoted as MXene/COF mixture; **Fig. S22C, D**) were compared as CDI electrode materials under the same conditions as the MXene@COF 2D heterostructure. The experimental results in **Table S2** demonstrate that even though the MXene/COF hybrid and MXene/COF mixture have the same components as the MXene@COF heterostructure, their CDI properties are greatly inferior to those of the MXene@COF heterostructure. We ascribe the high performance of the unique MXene@COF 2D heterostructure to its structural advantages, as it provides

a larger SSA, well-patterned COF nanoarrays, and better electron conductivity. Moreover, we also think that the heterointerface optimization will further endow the inner MXene nanosheets with strong oxidation resistance, which is highly important for practical applications. Therefore, cycling stability, a critical factor for evaluating the practicality of a CDI electrode, has been further investigated. As reported previously, pure MXenes are not very stable in environments containing water and oxygen. In this case, the MXene electrode is easily oxidized during long-term CDI cycling in a practical saline water containing dissolved oxygen, therefore the CDI performance of MXene manifestly decreases after only 20 cycles (**Fig. 4D**). By contrast, owing to the optimal heterointerface, the MXene@COF heterostructure can effectively avoid corrosion in practical saline water, resulting in a good structural stability without obvious performance deteriorating even after 100 cycles (**Fig. 4D**), demonstrating the strong oxidation resistance of MXene obtained by our method. Furthermore, the XRD pattern (**Fig. S23A**), N_2 adsorption–desorption isotherm (**Fig. S23B**), morphological observations (**Fig. S23C,D**), and EIS Nyquist plots (**Fig. S24**) of the MXene@COF heterostructure confirm its excellent structural stability after 20 CDI cycles in oxygenated saline water.

To further understand the importance of heterointerface optimization for the enhanced CDI performance of the MXene@COF heterostructure, DFT calculations were performed to study the interaction between MXene and COF (see Computational Method in the Supporting Information).[30] The calculated differential charge density of MXene@COF indicates interfacial electronic coupling between the MXene and COF surfaces (**Fig. S25A**). Furthermore, the microscopic structure of the MXene@COF was also simulated in the absence and presence of Na^+ to elucidate the charge transfer process during desalination or regeneration. When Na^+ is attached to the MXene@COF interface, the projected density of states in **Fig. S25B** shows that the MXene band is shifted leftward, toward lower energy relative to the Fermi level of the MXene@COF heterostructure, suggesting that electron transfer occurs between MXene and COF. The strong interaction between MXene and COF with enhanced charge separation contributes to the extremely high desalination performance. Further details are under investigation.

Conclusion

In summary, we developed an optimal heterointerface for MXene@COF 2D heterostructures through inorganic-organic assembly of pre-modified MXene ($Ti_3C_2T_x$) nanosheets with DAAQ-TFP-COFs. As an emerging family of MXene–organic 2D heterostructures, the obtained core–shell heterostructure with well-designed heterointerface exhibits several advantages including a large SSA, hierarchical porous structure, and the extraordinary redox capacitive behavior of the COF nanoarrays, as well as a 2D architecture, good electrical conductivity, and the reversible ion intercalation/deintercalation ability of the MXene nanosheets. The obtained MXene@COF heterostructure shows a high CDI performance, including a maximum SAC of 53.1 mg g^{-1} and excellent cycling stability over 100 cycles in oxygen-containing saline water. Notably, the MXene@COF heterostructure greatly outperforms most state-of-the-art MXene materials, indicating the potential application of MXene–organic 2D heterostructures for electrochemical applications.

Author contributions

Shuaihua Zhang designed the research, synthesized the MXene@COF heterostructures and wrote the manuscript. Xingtao Xu co-designed the research, conducted the CDI experiments and co-wrote the manuscript. Xiaohong Liu fabricated the CDI devices and did the characterization experiments. Qian Yang collected the experimental data and assisted in writing the manuscript. Ningzhao Shang assisted in the measurement and analysis of the data. Xiaoxian Zhao performed CV, EIS and GCD measurements. Xiaohuan Zang assisted in the construction of the MXene@COF heterostructures. Chun Wang managed the synthetic plan. Zhi Wang co-managed the project and co-wrote the manuscript. Joseph G. Shapter helped to analysis the CDI data and edited the manuscript. Yusuke Yamauchi managed the project, planned the experiments and edited the manuscript.

Conflicts of interest

There are no conflicts of interest to declare.

Acknowledgement

This work was partially supported by the National Natural Science Foundation of China (51909066), the Scientific Research Foundation for the Returned Scholars of Hebei Province (C20200335), National Natural Science Foundation of Hebei Province (C2020204136), and the JST-ERATO Yamauchi Materials Space-Tectonics Project (Grant Number: JPMJER2003). Xingtao Xu thanks the support from JSPS Postdoctoral Fellowship for Overseas Researchers.

References

1. X. Xu, T. Yang, Q. Zhang, W. Xia, Z. Ding, K. Eid, A. M. Abdullah, M. Shahriar A. Hossain, S. Zhang, J. Tang, L. Pan and Y. Yamauchi, *Chem. Eng. J.*, 2020, **390**, 124493.
2. J. Guo, X. Xu, J. P. Hill, L. Wang, J. Dang, Y. Kang, Y. Li, W. Guan and Y. Yamauchi, *Chem. Sci.*, 2021, **12**, 10334-10340.
3. G. Wang, T. Yan, J. Zhang, L. Shi and D. Zhang, *Environ. Sci. Technol.*, 2020, **54**, 8411-8419.
4. D.-H. Nam, M. A. Lumley and K.-S. Choi, *ACS Energy Lett.*, 2021, **6**, 1034-1044.
5. K. Wang, Y. Liu, Z. Ding, Z. Chen, X. Xu, M. Wang, T. Lu and L. Pan, *Chem. Eng. J.*, 2022, **433**, 133578.
6. C. Li, S. Wang, G. Wang, S. Wang, X. Che, D. Li and J. Qiu, *Environ. Sci.: Water Res. Technol.*, 2020, **6**, 303-311.
7. Y. Li, Y. Liu, M. Wang, X. Xu, T. Lu, C. Q. Sun and L. Pan, *Carbon*, 2018, **130**, 377-383.
8. P. Srimuk, X. Su, J. Yoon, D. Aurbach and V. Presser, *Nat. Rev. Mater.*, 2020, **5**, 517–538.
9. W. Shi, X. Liu, T. Deng, S. Huang, M. Ding, X. Miao, C. Zhu, Y. Zhu, W. Liu and F. Wu, *Adv. Mater.*, 2020, **32**, 1907404.
10. M. Mao, T. Yan, G. Chen, J. Zhang, L. Shi and D. Zhang, *Environ. Sci. Technol.*, 2020, **55**, 730-737.
11. Z. Wang, X. Xu, J. Kim, V. Malgras, R. Mo, C. Li, Y. Lin, H. Tan, J. Tang, L. Pan, Y. Bando, T. Yang and Y. Yamauchi, *Mater. Horiz.*, 2019, **6**, 1433-1437.
12. W. Zhang, A. Arramel, P. K. J. Wong, L. Zhang, J. Zheng, W. Zhang, H. Zhang, X. Yan, J. Qi and J. Li, *J. Mater. Chem. A*, 2020, **8**, 14653-14660.

13. S. Huo, Y. Zhao, M. Zong, B. Liang, X. Zhang, I. U. Khan, X. Song and K. Li, *J. Mater. Chem. A*, 2020, **8**, 2505-2517.

14. X. Xu, J. Tang, Y. V. Kaneti, H. Tan, T. Chen, L. Pan, T. Yang, Y. Bando and Y. Yamauchi, *Mater. Horiz.*, 2020, **7**, 1404-1412.

15. P. Srimuk, M. Zeiger, N. Jäckel, A. Tolosa, B. Krüner, S. Fleischmann, I. Grobelsek, M. Aslan, B. Shvartsev and M. E. Suss, *Electrochim. Acta*, 2017, **224**, 314-328.

16. W. Bao, X. Tang, X. Guo, S. Choi, C. Wang, Y. Gogotsi and G. Wang, *Joule*, 2018, **2**, 778-787.

17. P. Srimuk, F. Kaasik, B. Krüner, A. Tolosa, S. Fleischmann, N. Jäckel, M. C. Tekeli, M. Aslan, M. E. Suss and V. Presser, *J. Mater. Chem. A*, 2016, **4**, 18265-18271.

18. J. Ma, Y. Cheng, L. Wang, X. Dai and F. Yu, *Chem. Eng. J.*, 2020, **384**, 123329.

19. J. Ai, J. Li, K. Li, F. Yu and J. Ma, *Chem. Eng. J.*, 2021, **408**, 127256.

20. S. Anwer, D. H. Anjum, S. Luo, Y. Abbas, B. Li, S. Iqbal and K. Liao, *Chem. Eng. J.*, 2021, **406**, 126827.

21. H. Shao, K. Xu, Y.-C. Wu, A. Iadecola, L. Liu, H. Ma, L. Qu, E. Raymundo-Piñero, J. Zhu, Z. Lin, P.-L. Taberna and P. Simon, *ACS Energy Lett.*, 2020, **5**, 2873-2880.

22. N. Kurra, M. Alhabeb, K. Maleski, C.-H. Wang, H. N. Alshareef and Y. Gogotsi, *ACS Energy Lett.*, 2018, **3**, 2094-2100.

23. M. Naguib, V. N. Mochalin, M. W. Barsoum and Y. Gogotsi, *Adv. Mater.*, 2014, **26**, 992-1005.

24. Z. Ding, X. Xu, J. Li, Y. Li, K. Wang, T. Lu, M. S. A. Hossain, M. A. Amin, S. Zhang, L. Pan and Yusuke Yamauchi, *Chem. Eng. J.*, 2022, **430**, 133161.

25. J. Peng, X. Chen, W. Ong, X. Zhao and N. Li, *Chem*, 2019, **5**, 18-50.

26. J. Yan, C. E. Ren, K. Maleski, C. B. Hatter, B. Anasori, P. Urbankowski, A. Sarycheva and Y. Gogotsi, *Adv. Funct. Mater.*, 2017, **27**, 1701264.

27. Z. Chen, X. Xu, Z. Ding, K. Wang, X. Sun, T. Lu, M. Konarova, M. Eguchi, J. G. Shapter, L. Pan and Y. Yamauchi, *Chem. Eng. J.*, 2021, **407**, 127148.

28. Q. Li, X. Xu, J. Guo, J. P. Hill, H. Xu, L. Xiang, C. Li, Y. Yamauchi and Y. Mai, *Angew. Chem. Int. Ed.*, 2021, **60**, 26528-26534.

29. X. Liu, S. Zhang, G. Feng, Z.-G. Wu, D. Wang, M. D. Albaqami, B. Zhong, Y. Chen, X. Guo and X. Xu, Y. Yamauchi, *Chem. Mater.*, 2021, **33**, 1657–1666.

30. R. Meng, Q. Deng, C. Peng, B. Chen, K. Liao, L. Li, Z. Yang, D. Yang, L. Zheng, C. Zhang and J. Yang, *Nano Today*, 2020, **35**, 100991.

31. H. Wang, C. Qian, J. Liu, Y. Zeng, D. Wang, W. Zhou, L. Gu, H. Wu, G. Liu and Y. Zhao, *J. Am. Chem. Soc.*, 2020, **142**, 4862-4871.

32. D. Guo, F. Ming, D. B. Shinde, L. Cao, G. Huang, C. Li, Z. Li, Y. Yuan, M. N. Hedhili, H. N. Alshareef and Z. Lai, *Adv. Funct. Mater.*, 2021, **31**, 2101194.

33. X. Xu, S. Zhang, J. Tang, L. Pan, M. Eguchi, J. Na and Y. Yamauchi, *EnergyChem*, 2020, **2**, 100043.

34. C. Yang, Q. Tan, Q. Li, J. Zhou, J. Fan, B. Li, J. Sun and K. Lv, *Appl. Catal. B.*, 2020, **268**, 118738.

35. H. Liao, X. Guo, P. Wan and G. Yu, *Adv. Funct. Mater.*, 2019, **29**, 1904507.

36. Y. Shi, B. Li, Q. Zhu, K. Shen, W. Tang, Q. Xiang, W. Chen, C. Liu, J. Luo and S. Yang, *Adv. Energy Mater.*, 2020, **10**, 1903534.

37. L. Jiao, C. Zhang, C. Geng, S. Wu, H. Li, W. Lv, Y. Tao, Z. Chen, G. Zhou, J. Li, G. Ling, Y. Wan and Q. Yang, *Adv. Energy Mater.*, 2019, **9**, 1900219.

38. C. R. DeBlase, K. E. Silberstein, T.-T. Truong, H. D. Abruña and W. R. Dichtel, *J. Am. Chem. Soc.*, 2013, **135**, 16821-16824.

39. C. R. DeBlase, K. Hernández-Burgos, K. E. Silberstein, G. G. Rodríguez-Calero, R. P. Bisbey, H. D. Abruña and W. R. Dichtel, *ACS Nano*, 2015, **9**, 3178-3183.

40. S. Zhang, W. Xia, Q. Yang, Y. Valentino Kaneti, X. Xu, S. M. Alshehri, T. Ahamad, M. S. A. Hossain, J. Na, J. Tang and Y. Yamauchi, *Chem. Eng. J.*, 2020, **396**, 125154.

41. W. Yang, B. Huang, L. Li, K. Zhang, Y. Li, J. Huang, X. Tang, T. Hu, K. Yuan and Y. Chen, *Small Methods*, 2020, **4**, 2000434.

42. N. Wang, H. Wang, Y. Wang, Y. Wei, J. Si, A. C. Y. Yuen, J. Xie, B. Yu, S. Zhu, H. Lu, W. Yang, Q. N. Chan and G. Yeoh, *ACS Appl. Mater. Interfaces*, 2019, **11**, 40512-40523.

43. A. Khayum M, V. Vijayakumar, S. Karak, S. Kandambeth, M. Bhadra, K. Suresh, N. Acharambath, S. Kurungot and R. Banerjee, *ACS Appl. Mater. Interfaces*, 2018, **10**, 28139-28146.

44. Y. Li, Z. Ding, X. Zhang, J. Li, X. Liu, T. Lu, Y. Yao and L. Pan, *J. Mater. Chem. A*, 2019, **7**, 25305-25313.

45. A. P. Cote, H. M. El-Kaderi, H. Furukawa, J. R. Hunt and O. M. Yaghi, *J. Am. Chem. Soc.*, 2007, **129**, 12914-12915.

46. M. Torkamanzadeh, L. Wang, Y. Zhang, Ö. Budak, P. Srimuk and V. Presser, *ACS Appl. Mater. Interfaces*, 2020, **12**, 26013-26025.

47. P. Srimuk, J. Halim, J. Lee, Q. Tao, J. Rosen and V. Presser, *ACS Sustainable Chem. Eng.*, 2018, **6**, 3739-3747.